



Relativistic Reflection and Reverberation in GX 339–4 with NICER and NuSTAR

Jingyi Wang¹, Erin Kara¹, James F. Steiner^{1,2}, Javier A. García^{3,4}, Jeroen Homan^{5,6}, Joseph Neilsen⁷, Grégoire Marcel⁷, Renee M. Ludlam³, Francesco Tombesi^{8,9,10,11}, Edward M. Cackett¹², and Ron A. Remillard¹

¹ MIT Kavli Institute for Astrophysics and Space Research, MIT, 70 Vassar Street, Cambridge, MA 02139, USA

² Harvard-Smithsonian Center for Astrophysics, 60 Garden Street, Cambridge, MA 02138, USA

³ Cahill Center for Astronomy and Astrophysics, California Institute of Technology, Pasadena, CA 91125, USA

⁴ Remeis Observatory & ECAP, Universität Erlangen-Nürnberg, D-96049 Bamberg, Germany

⁵ Eureka Scientific, Inc., 2452 Delmer Street, Oakland, CA 94602, USA

⁶ SRON, Netherlands Institute for Space Research, Sorbonnelaan 2, 3584 CA Utrecht, The Netherlands

⁷ Department of Physics, Villanova University, 800 Lancaster Avenue, Villanova, PA 19085, USA

⁸ Department of Astronomy, University of Maryland, College Park, MD 20742, USA

⁹ X-ray Astrophysics Laboratory, NASA/Goddard Space Flight Center, Greenbelt, MD 20771, USA

¹⁰ Department of Physics, University of Rome “Tor Vergata,” Via della Ricerca Scientifica 1, I-00133, Rome, Italy

¹¹ INAF—Astronomical Observatory of Rome, via Frascati 33, I-00044, Monte Porzio Catone (Rome), Italy

¹² Department of Physics & Astronomy, Wayne State University, 666 West Hancock Street, Detroit, MI 48201, USA

Received 2019 October 2; revised 2020 June 17; accepted 2020 June 19; published 2020 August 11

Abstract

We analyze seven Neutron Star Interior Composition Explorer (NICER) and Nuclear Spectroscopic Telescope Array epochs of the black hole X-ray binary GX 339–4 in the hard state during its two most recent hard-only outbursts in 2017 and 2019. These observations cover the 1–100 keV unabsorbed luminosities between 0.3% and 2.1% of the Eddington limit. With NICER’s negligible pileup, high count rate, and unprecedented time resolution, we perform a spectral-timing analysis and spectral modeling using relativistic and distant reflection models. Our spectral fitting shows that as the inner disk radius moves inward, the thermal disk emission increases in flux and temperature, the disk becomes more highly ionized, and the reflection fraction increases. This coincides with the inner disk increasing its radiative efficiency around $\sim 1\%$ Eddington. We see a hint of the hysteresis effect at $\sim 0.3\%$ of Eddington; the inner radius is significantly truncated during the rise ($>49R_g$), while only a mild truncation ($\sim 5R_g$) is found during the decay. At higher frequencies (2–7 Hz) in the highest-luminosity epoch, a soft lag is present whose energy dependence reveals a thermal reverberation lag with an amplitude similar to previous findings for this source. We also discuss the plausibility of the hysteresis effect and the debate of the disk truncation problem in the hard state.

Unified Astronomy Thesaurus concepts: Black holes (162); High energy astrophysics (739); Astrophysical black holes (98); Stellar mass black holes (1611); Low-mass X-ray binary stars (939); X-ray astronomy (1810)

1. Introduction

Black hole astrophysics can be regarded as a fundamental tool in providing information about the accretion and ejection physics in the strongest gravity regime in the universe. The standard picture for an accreting black hole system involves an accretion disk that emits as a multitemperature blackbody (~ 0.1 – 2 keV) and a hot (hundreds of keV) plasma called an X-ray “corona” whose nature is still not clear (see Done et al. 2007 for a review). Inverse Compton scattering of the thermal photons from the accretion disk off free electrons in the corona generates a Comptonization component, usually modeled by a power-law spectrum with a high-energy cutoff. A fraction of the Comptonized photons may shine back onto the disk. The interaction of these photons with the material in the accretion disk, including Compton scattering, photoelectric absorption followed by fluorescent line emission, or Auger de-excitation, produces a reflection spectrum (García et al. 2014; Bambi 2017). If the reflection happens very close to the black hole, then the local spectrum is expected to be smeared by relativistic effects (Fabian et al. 1989). For this reason, X-ray reflection spectroscopy provides a powerful diagnostic tool for investigating the dynamics and geometry of the accretion disk. The modeling of reflection features is being used to measure the spin, inclination angle, and ionization in a variety of black hole systems (see Reynolds 2013 for a review).

The brightest outburst of black hole binaries (BHBs) can be described by a hysteresis pattern in the hardness–intensity diagram (HID; e.g., Fender et al. 2004, and see the lower panel in Figure 1). The majority of BHBs spend most of their time in the quiescent state when the accretion rate onto the black hole is low and the X-ray emission is weak, often undetected. The X-ray emission is dominated by the Comptonization component in the hard state, while the luminosity increases until it starts its transition to the soft state where the thermal disk component dominates. The luminosity gradually drops, and the source makes the transition back to the hard state and then to quiescence (Remillard & McClintock 2006). Sometimes, the outbursts are hard-only when the BHB stays in the hard state and the transition to the soft state does not take place (Tetarenko et al. 2016).

It is of central importance to determine the evolution of physical properties in the accretion disk and corona because it could provide us with insights into the accretion process, the nature of the corona and jet, and the mechanisms governing state transitions.

The low-mass X-ray binary GX 339–4 goes into outburst cycles typically every 2–3 yr (Tetarenko et al. 2016). A near-infrared (NIR) study in Heida et al. (2017) constrained the mass of the black hole to $2.3M_\odot < M_{\text{BH}} < 9.5M_\odot$; the distance to GX 339–4 is difficult to accurately measure, and only a lower limit of ~ 5 kpc can be derived. In this work, to estimate the

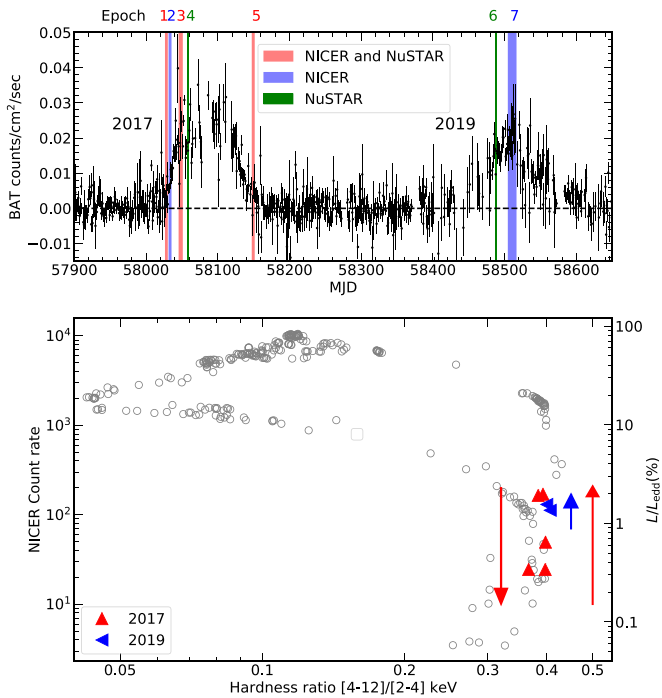


Figure 1. (Upper) Swift/BAT light curve (15–50 keV) of GX 339–4 during 2017 and 2019 hard-only outbursts, with seven epochs we chose labeled using vertical shaded regions. Different color coding represents the data availability in each epoch. (Lower) NICER HID, where the hardness ratio is defined as the count ratio of the hard band (4–12 keV) and the soft band (2–4 keV). The gray circles are simulated from RXTE PCU-2 spectral data in the 2002–2003 outburst by first fitting with a Comptonized disk-blackbody model from 3 to 45 keV. For each data set, the best-fitting model was then convolved with the NICER response matrix to produce the simulated HID track, which is shown.

luminosity in units of Eddington limit, the distance is assumed to be 8 kpc, and the mass is $10 M_{\odot}$ to make comparisons with previous results in the literature more convenient.

In Wang-Ji et al. (2018), we analyzed the X-ray spectra of this source during the 2013 and 2015 outbursts with the Nuclear Spectroscopic Telescope Array (NuSTAR; Harrison et al. 2013) and the Neil Gehrels Swift Observatory (Swift). In this paper, we present a new analysis of the 2017 and 2019 outbursts with NuSTAR and the Neutron Star Interior Composition Explorer (NICER; Gendreau et al. 2016). These two recent outbursts are hard-only outbursts because GX 339–4 did not make the transition from the hard state to the soft state, as it does during its brightest outbursts. García et al. (2019) recently analyzed the 2017 outburst using NuSTAR and complementary Swift data. Their best-performing spectral models suggest that an approximation of the corona by two lamppost illuminators offered a better description of the reflection and continuum data than the usually adopted lamppost plus distant neutral reflection.

The answer to the question of whether the disk in BHBs becomes truncated in the luminous hard state has been controversial for several years, and GX 339–4, as an archetypical BHB, has been extensively studied with reflection spectroscopy (e.g., Tomsick et al. 2008; Petrucci et al. 2014; Plant et al. 2015; Basak & Zdziarski 2016; Jiang et al. 2019). Early observations of the disk truncation radius in the luminous hard state were controversial because pileup could affect the shape of the iron line (Miller et al. 2006; Reis et al. 2008; Done & Diaz Trigo 2010). Recent analysis with RXTE (García et al. 2015) and NuSTAR (Wang-Ji et al. 2018) has allowed for a

more reliable determination of the reflection spectrum and suggested that the disk truncation level was below $\sim 10R_g$ ($R_g = GM_{\text{BH}}/c^2$) when $L > 1\%L_{\text{Edd}}$. However, debate still ensues about the choice of reflection model and underlying continuum (Dzielał et al. 2019; Mahmoud et al. 2019).

With reflection spectroscopy focusing on the time-integrated energy spectra, Fourier timing techniques have been developed more recently, which could quantify the multitimescale variability and the corresponding time delays between energy bands (see Uttley et al. 2014 for a review). The reverberation signal is the time lag introduced by light travel time differences between observed variations in the direct power law and the corresponding changes in the reflection spectrum. The first significant reverberation lag was detected in the active galactic nucleus (AGN) 1H 0707–495 (Fabian et al. 2009), with soft-excess emission lagging the continuum-dominated band above 7×10^{-4} Hz (equivalent to timescales shorter than 30 minutes). Later, other reverberation signatures, lags at the iron K emission line at ~ 6.4 keV, were revealed by lag-energy spectra (Zoghbi et al. 2012; Kara et al. 2016), which self-consistently follow the reflection picture. For BHBs, the detection of reverberation lags is more difficult because the number of received photons per light travel time (determined by R_g , which is different by a factor of 10^5 or more) is much smaller. Disk thermal reverberation lags were first detected for GX 339–4 (Uttley et al. 2011; De Marco et al. 2015) and later also in H1743–322 (De Marco & Ponti 2016).

High-frequency soft lags have been interpreted as due to reverberation. However, directly converting the amplitude of the time delays to a light travel distance has led to suggestions that the corona–disk distance could be hundreds of R_g , whereas X-ray reflection spectroscopy suggests a small disk truncation of $< 10R_g$ (e.g., García et al. 2015). This highlights another aspect of the truncation debate in the hard state. Therefore, with NICER’s superior time resolution and no pileup, we want to measure the reverberation lag and compare to the energy spectral fitting and the lag measured with XMM-Newton data (De Marco et al. 2015, 2017).

Besides reverberation signatures, it has long been known that there are fairly ubiquitous hard lags at low temporal frequencies (below $\sim 300M_{\odot}/M$ Hz), both in AGNs (Papadakis et al. 2001; McHardy et al. 2004, 2007; Arévalo & Uttley 2006) and BHBs (Van der Klis et al. 1987; Miyamoto & Kitamoto 1989; Vaughan et al. 1994; Nowak et al. 1999). These hard lags are difficult to explain with models invoking light travel time delays. For instance, Compton upscattering of photons in the corona would require a corona that is extremely large to match the large amplitude of the hard lags (Nowak et al. 1999); the reverberation delay of reflection from a disk cannot explain the sign of the lags (Cassatella et al. 2012). Therefore, a nonreverberation explanation is needed, which is also consistent with the fact that the corresponding lag-energy spectra only display a featureless energy dependence, without any reflection features. The most promising interpretation at present is propagating the mass accretion rate fluctuation first proposed by Lyubarskii (1997).

This paper is organized as follows. Section 2 describes the observations and data reduction, and Section 3 provides the details of the energy spectral fitting. We present the time lag analysis with NICER data in Section 4 and a discussion in Section 5, and we summarize the results in Section 6.

Table 1
NICER and NuSTAR Observations in the 2017 and 2019 Outburst Cycles, Exposure Times, and Dates

Outburst	Epoch	L/L_{edd} (%)	NICER				NuSTAR			
			ObsID ^a	Date	Exp.(ks)	Counts s ⁻¹	ObsID	Date	Exp.(ks)	Counts s ⁻¹
2017	1	0.3	03-05	10/01–10/04	7.8	24.5	80302304002	10/02	21.5	2.0
	2	0.6	07-10	10/06–10/09	5.0	49.4
	3	1.8	12-15	10/20–10/23	7.4	164.6	80302304004	10/25	18.0	22.8
	4	2.1	80302304005	11/02	18.9	16.9
	5	0.3	27-29	01/31–02/02 2018	3.9	24.5	80302304007	01/30 2018	29.0	3.2
2019	6	1.4	90401369004	01/05	3.6	14.4
	7	1.6	39–47	01/22–02/02	19.3	130.6

Notes. Luminosity is calculated using the unabsorbed flux between 1 and 100 keV, assuming a distance of 8 kpc and a black hole mass of $10 M_{\odot}$. The count rates are for the fitted energy ranges, i.e., 0.4–10 keV for NICER and 3–79 keV for NuSTAR.

^a ObsIDs for NICER are 11330101xx.

2. Observations and Data Reduction

In 2017 September, GX 339–4 entered an outburst after an optical brightening (Russell et al. 2017a). Then, multiwavelength observations were triggered, showing a flux rise in both radio (Russell et al. 2017b) and X-ray (Gandhi et al. 2017). NICER monitored GX 339–4 on a 1–2 day cadence from 2017 September 29 to October 23 and 2018 January 23 to February 26, with the gap caused by solar angle constraints. In 2019, NICER made observations from January 22 to February 2, catching the peak of another hard-only outburst (see Epoch 7 in Figure 1). The relevant ObsIDs are 1133010101 through 1133010147.

We adopt the same 2017 NuSTAR data set, including four observations (ObsIDs 80302304002 through 80302304007), as in García et al. (2019), in which simultaneous Swift observations are used to cover the soft energy band. As for the 2019 outburst, NuSTAR made two target-of-opportunity observations. Only the latter one on 2019 January 5 is used (ObsID 90401369004) because of the short exposure time of the other (<1 ks). The Swift/BAT (Krimm et al. 2013) light curve and the NICER HID are shown in Figure 1, where the background gray HID track is simulated from RXTE spectra in GX 339–4’s 2002–2003 outburst.

The NICER data are processed with NICER data analysis software (NICERDAS) version 2017-09-06_V002 and CALDB version 20170814. We use the standard filtering criteria: the pointing offset is less than $54''$, and the pointing direction is more than 40° away from the bright Earth limb, more than 30° away from the dark Earth limb, and outside the South Atlantic Anomaly. In addition, we select events that are not flagged as “overshoot” or “undershoot” resets (EVENT_FLAGS = bxxxx00) or forced triggers (EVENT_FLAGS = bx1x000). A “trumpet” filter is also applied to filter out known background events (Bogdanov 2019). We select NICER observations with at least one good time interval (GTI) longer than 60 s and extract individual spectra for each GTI. The cleaned events are barycenter-corrected using the FTOOL `barycorr`. Our data sets were comprised of observations taken during observatory day and night times. The daytime data gains were corrected for optical loading due to a light leak on the instrument. Calibration uncertainties from these were reduced by correcting the spectra using residuals of a power-law fit to the Crab Nebula, a method referred to as “Crab correction” (Ludlam et al.

2018). The background spectra are obtained using NICER background model 3C50_RGv5 (R. A. Remillard et al. 2020, in preparation). To boost signal-to-noise ratios, we combine close-in-time individual spectra with similar hardness ratios ($[4-12]/[2-4]$ keV) and count rates (see Table 1). The spectra are then binned with a minimum count of 1 channel⁻¹, and the oversampling factor is 3. The fitted energy range is 0.4–10 keV because the spectra become background-dominated above 10 keV. The response matrices we use in spectral fitting are `nicer_v1.02.rmf` and `ni_xrcall_onaxis_v1.02.arf`. For the purpose of timing analysis, the light-curve segment length is 10 s with 0.001 s bins, which covers frequencies from 0.1 to 500 Hz.

NuSTAR data are reduced using data analysis software (NUSTARDAS) 1.8.0 and CALDB v20170817. Source spectra are extracted from $60''$ circular extraction regions centered on the source position and background spectra from $100''$ off-source circular regions. The NuSTAR data taken during 2019 (ObsID 90401369004) are only available in observation mode 06 because the source was Sun-constrained, so a specific NUSTARDAS software module, “nusplitsc,” is used to generate event files for different combinations of the three star tracker camera units. The source is extracted from $120''$ circular regions, background from $100''$ off-source circular regions. The spectra are then generated by the standard “nuproducts” task. The spectra for different combinations of the three star tracker camera units in ObsID 90401369004 are combined using the FTOOL “addspec.” The FPMA/B spectra are binned with a minimum signal-to-noise of 5 bin⁻¹, and the oversampling factor was 3. The fitted energy range is 3–79 keV.

With the availability of data, we choose seven epochs in total to cover the two hard-only outbursts (see Figure 1 and Table 1). Epochs 1–4 were taken during the rising phase of the 2017 outburst, reaching a maximal 1–100 keV unabsorbed luminosity of $2.1\% L_{\text{Edd}}$, assuming a distance of 8 kpc and a black hole mass of $10 M_{\odot}$, while Epoch 5 was in the decay phase, with a luminosity similar to Epoch 1. Epochs 6 and 7 were both in the rising phase of the 2019 outburst, and the peak luminosity ($1.6\% L_{\text{Edd}}$) is slightly lower than the peak in 2017.

All of the uncertainties quoted in this paper are for a 90% confidence range, unless otherwise stated. All spectral fitting is done with XSPEC 12.10.1f (Arnaud 1996). In all of the fits, we use the *wilm* set of abundances (Wilms et al. 2000) and *vern* photoelectric cross sections (Verner et al. 1996). The fitting

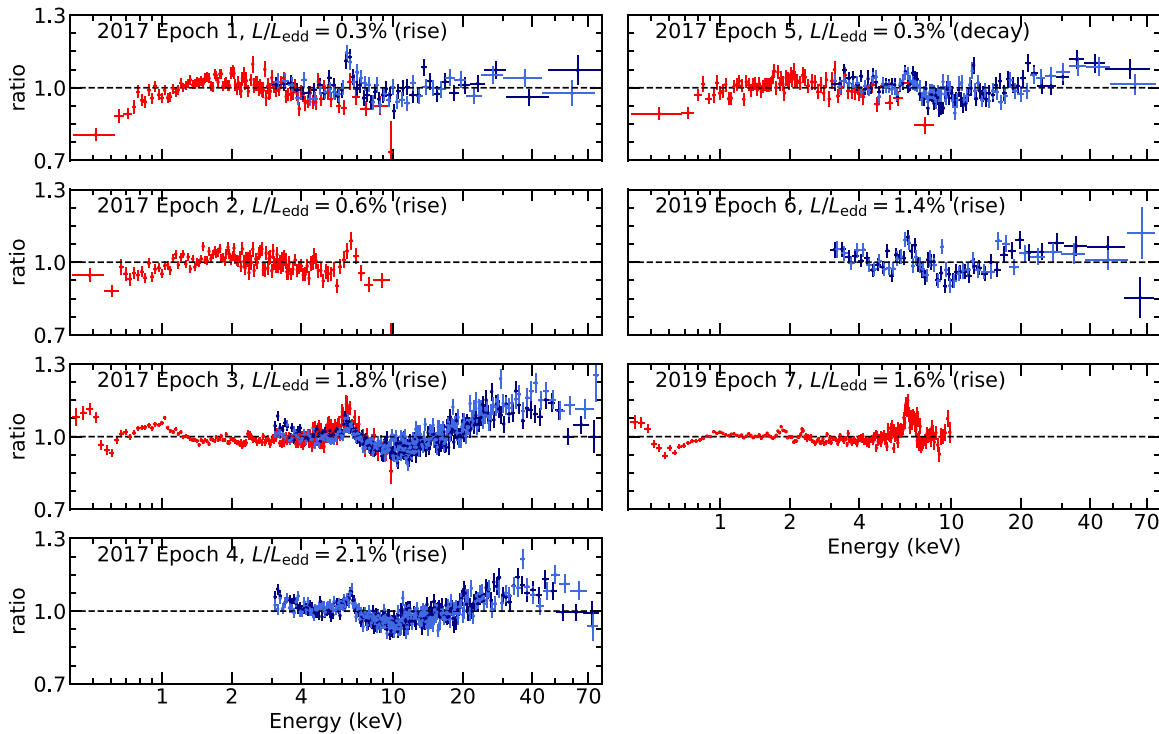


Figure 2. Data-to-model ratio for the simultaneous fit with the absorbed power-law model (`Tbabs*crabcorr*powerlaw`). The iron line complex around 6.4 keV is prominent in all epochs, and the Compton hump above 20 keV is also present in Epochs 3 and 4 with the highest luminosities. Red: NICER; navy: NuSTAR/FPMA; blue: NuSTAR/FPMB.

statistics is PG-statistics,¹³ for Poisson data with a Gaussian background.

3. Spectral Fitting

3.1. Toward the Final Model

In order to assess the reflection features, we first fit the 15 spectra (five NICER spectra and 10 NuSTAR spectra accounting for both FPMA and FPMB) simultaneously with an absorbed power-law model (`Tbabs*crabcorr*powerlaw` in XSPEC notation). The cross-calibration between NICER and NuSTAR is carried out by the model `crabcorr` (Steiner et al. 2010), which could multiply each model spectrum by a power law, applying corrections to both the slope of the power law via the parameter $\Delta\Gamma$ and normalization. In this way, the responses of different detectors are cross-calibrated to return the same normalizations and power-law slopes for the Crab. The column density N_{H} is tied, while the photon index Γ is free to vary between epochs. The resulting data-to-model ratios are shown in Figure 2, where the iron line complex is prominent in all epochs, and the Compton hump can also be seen in some of the spectra. This fit gives a Galactic column density of $N_{\text{H}} \sim 5.8 \times 10^{21} \text{ cm}^{-2}$.

Next, we perform a simultaneous fit to all seven epochs using the relativistic reflection model `relxillCp`. In XSPEC notation, the model is `Tbabs*crabcorr*relxillCp`. The reflection model `relxillCp` includes both the original continuum emission from the “corona” and the reprocessed emission from the disk. The coronal emission is described by `nthcomp` with the seed photons originating from the disk

(Zdziarski et al. 1996; Życki et al. 1999). The spin a_* has been measured to be high for GX 339–4 (e.g., >0.97 in Ludlam et al. 2015 and $0.95_{-0.08}^{+0.02}$ in Parker et al. 2016). Therefore, the spin parameter is fixed at the maximal value of 0.998 to allow the inner disk radius to fit to any physically allowed value. We find that the electron temperatures in the corona (kT_e) can only be constrained to have lower limits, i.e., pegged at the maximal value, so we fix $kT_e = 400 \text{ keV}$ in the subsequent fittings; we also confirm that allowing kT_e to vary does not improve the fit ($\Delta\text{PG-stat} < 1$), and other parameter values stay the same. With regard to the emissivity profile, we choose the canonical profile of $\propto r^{-3}$ (emissivity index $q = 3$), and we explore these effects in Section 3.4. This fit results in PG-statistics/degrees of freedom ($\text{dof} = 7702/5827 = 1.32$).

However, similar to earlier works on GX 339–4 (García et al. 2015; Wang-Ji et al. 2018; Jiang et al. 2019), we find that a single component of relativistic reflection could not fully describe the iron line region (see the upper panel in Figure 3 showing the zoom-in residuals around the iron line of NICER data in Epoch 7 as an example), and that an extra distant reflector modeled by `xillverCp` could solve this problem. Within `xillverCp`, parameters describing the properties of the corona (photon index Γ , electron temperature kT_e) and the system (inclination i , Fe abundance A_{Fe}) are tied to those in `relxillCp`. Also, the reflector is assumed to be close to neutral, i.e., $\log \xi (\text{erg cm s}^{-1}) = 0$. We find that if $\log \xi$ is free to vary, the PG-stat decreases by 11 with seven fewer parameters, which is not significant; the constraints on $\log \xi$ are loose, and the other parameter values are not affected. These setups only add one extra free parameter per epoch, namely the normalization of `xillverCp`. With this model (`Tbabs*crabcorr*(relxillCp+xillverCp)`), the PG-statistics reduces by 368 with seven fewer dof, and the

¹³ <https://heasarc.gsfc.nasa.gov/xanadu/xspec/manual/XSappendixStatistics.html>

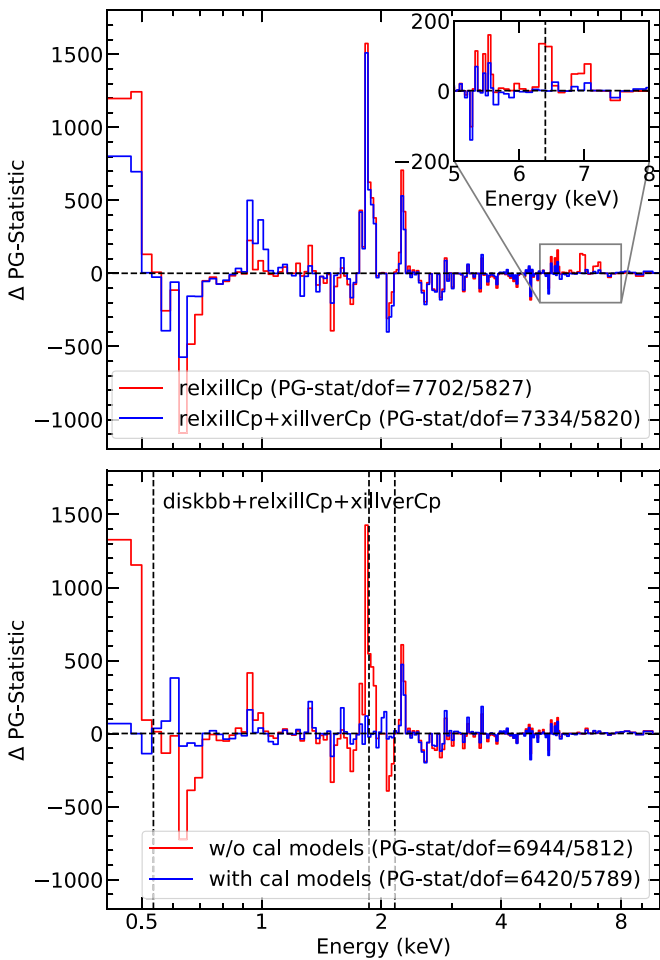


Figure 3. Residuals for NICER data in Epoch 7 from simultaneous fits with different models. (Upper) Reflection from a distant reflector is needed to fully describe the iron line region. (Lower) red: without the phenomenological calibration models, i.e., $T_{\text{babs}} * \text{crabcorr} * [\text{model shown}]$; blue: with the calibration models, i.e., $T_{\text{babs}} * \text{crabcorr} * ([\text{model shown}] + \text{Gaussian}) * \text{edge} * \text{edge}$. The best-fit energies in the calibration models are also plotted with vertical dashed lines. Notice that the PG-statistics values are for simultaneous fits, even though only the NICER data in Epoch 7 are shown.

residuals around the iron line are largely diminished, as expected.

As shown in Figure 3 (upper), strong features at soft energies (< 3 keV) are still present. A straightforward explanation is a thermal disk component, so we try the model of $\text{crabcorr} * T_{\text{babs}} * (\text{diskbb} + \text{relxillCp} + \text{xillverCp})$. Since the disk component is not visible in NuSTAR’s energy range, the disk components in Epochs 4 and 6, which consist of NuSTAR data alone, are tied to those in Epochs 3 and 7, respectively. For the other five epochs, disk temperatures in Epochs 1 and 5 with the lowest luminosities ($\sim 0.3\% L_{\text{Edd}}$) are pegged at the lowest value allowed, so we fix the disk temperature at a reasonably low value of 50 eV in these two epochs and only let the normalizations free to obtain a putative estimate of the unscattered flux from the disk component, i.e., disk photons that are not scattered when passing through the corona. In Epochs 2, 3, and 7 with luminosities above $0.5\% L_{\text{Edd}}$, the disk temperature is determined to be 100–200 eV based on NICER data. This model further reduces PG-statistics by 390 with eight extra free parameters, resulting in PG-statistics/dof = $6944/5812 = 1.19$.

We notice that there are still some large residuals at soft energies (see Figure 3, lower panel). The most noticeable features include edge-like shapes near ~ 0.5 and ~ 2.2 keV and Gaussian-like emission around 1.8 keV. These energies correspond to features in NICER’s effective area versus energy, where 0.5, 1.8, and 2.2 keV features are attributed to oxygen, silicon, and gold, respectively. Therefore, we have reason to believe that these remaining features come from NICER’s calibration systematics, and we model them empirically in our work. We suggest that observers be aware of such residuals and follow the latest analysis guidelines of the NICER analysis. The final model we adopt can be expressed as

$$\begin{aligned} & \text{crabcorr} * T_{\text{babs}} * (\text{diskbb} \\ & + \text{relxillCp} + \text{xillverCp} \\ & + \text{gaussian}) * \text{edge} * \text{edge}, \end{aligned}$$

where the gaussian and the two edge components are phenomenological models to account for residual calibration features. In each model, the energy is tied through the five epochs containing NICER data, while the other quantities (σ and norm in gaussian, τ_{max} in edge) can vary. This allows for potential attitude-dependent variations, which are not accounted for in the current response functions. In comparison with the fit without calibration models, the PG-stat/dof becomes $6420/5789 = 1.11$, decreasing by 524 with 23 fewer dof. We also emphasize that the parameters coming out of the reflection modeling are not changed when accounting for the calibration features. The residuals of NICER data in Epoch 7 for these two fits are shown in Figure 3 (lower), where the best-fit energies in calibration models are also plotted with vertical dashed lines. The (data–model)/error for all of the epochs and the model components are shown in the upper and lower portions of Figure 4. The best-fit parameters are presented in Table 2.

3.2. Global Parameters

In this simultaneous fit with ~ 5.2 million counts, the column density (in units of 10^{21} cm^{-2}) is constrained to be $N_{\text{H}} = 6.41^{+0.08}_{-0.09}$, which is consistent with previous X-ray reflection spectroscopy results including, e.g., the value determined by Suzaku (~ 6.8 in Tomsick et al. 2009; 4.7–6.7 in Petrucci et al. 2014), XMM-Newton (~ 7.0 in Basak & Zdziarski 2016), and Swift (4.1–6.9, Wang-Ji et al. 2018). From optical reddening, N_{H} is 6.0 ± 0.6 (Zdziarski et al. 1998), also consistent with our result.

We find that the inclination angle is $(38^{+2}_{-3})^\circ$, consistent with $\sim 40^\circ$ in Wang-Ji et al. (2018) and slightly smaller than $\sim 48^\circ$ in García et al. (2015). Previous reflection spectroscopy studies have constrained the inclination to $i = 30^\circ$ – 60° , with the exact value being model-dependent (García et al. 2015; Steiner et al. 2017). Also, our result is in agreement with the inclination found with Suzaku data ($36^\circ \pm 4^\circ$; Ludlam et al. 2015). In addition, the latest ellipsoidal light curve in the NIR band has shown that the binary inclination is $37^\circ < i < 78^\circ$ (Heida et al. 2017), whose lower limit is close to our result here. The inclination obtained with reflection spectroscopy is for the inner accretion disk and could possibly be different from the binary inclination.

Another global parameter in our simultaneous fit is the iron abundance, found to be $A_{\text{Fe}} = 4.08^{+0.15}_{-0.22}$ in solar units. This is still supersolar, and, as shown in García et al. (2015) and Wang-Ji et al. (2018), we confirm that this preference comes

Table 2
Best-fit Parameters for the Final Model $T_{\text{babs}} * \text{crabcorr} * (\text{diskbb} + \text{relxillCp} + \text{xillverCp} + \text{Gaussian}) * \text{edge} * \text{edge}$

Model	Parameter	Epoch 1	Epoch 2	Epoch 3	Epoch 4	Epoch 5	Epoch 6	Epoch 7
TBABS	N_{H} (10^{21} cm^{-2})				$6.41^{+0.08}_{-0.09}$			
RELXILLCP	a_*				0.988 (f)			
RELXILLCP	i (deg)				$37.6^{+2.9}_{-2.9}$			
RELXILLCP	A_{Fe}				$4.08^{+0.15}_{-0.22}$			
RELXILLCP	kT_{e} (keV)				400 (f)			
RELXILLCP	q				3 (f)			
GAUSSIAN	E (keV)				1.861 ± 0.011			
edge ₁	E (keV)				$2.161^{+0.025}_{-0.026}$			
edge ₂	E (keV)				$0.535^{+0.004}_{-0.003}$			
DISKBB	T_{in} (eV)	50 (f)	106^{+38}_{-52}	193 ± 5	...	50 (f)	...	178^{+20}_{-9}
DISKBB	Norm (10^3)	<600	11^{+64}_{-9}	$6.4^{+1.6}_{-1.2}$...	<950	...	$3.5^{+1.6}_{-1.1}$
DISKBB	F_{disk} ($10^{-13} \text{ erg cm}^{-2} \text{ s}^{-1}$)	<5.5	44 ± 14	867 ± 12	...	<8.7	...	301 ± 7
RELXILLCP	R_{in} (R_{ISCO})	>39.8	>28.5	<1.9	<1.8	$4.0^{+6.1}_{-0.7}$	<7.9	$3.1^{+0.9}_{-0.5}$
RELXILLCP	Γ	$1.564^{+0.007}_{-0.012}$	$1.547^{+0.017}_{-0.016}$	$1.514^{+0.028}_{-0.018}$	$1.528^{+0.024}_{-0.025}$	1.640 ± 0.018	$1.557^{+0.021}_{-0.010}$	$1.599^{+0.003}_{-0.008}$
RELXILLCP	$\log \xi$ (erg cm s^{-1})	$2.67^{+0.11}_{-0.64}$	$3.17^{+0.13}_{-0.09}$	$3.78^{+0.06}_{-0.05}$	$3.78^{+0.08}_{-0.11}$	<2.55	$3.12^{+0.25}_{-0.20}$	$2.84^{+0.06}_{-0.09}$
RELXILLCP	R_{f}	$0.024^{+0.027}_{-0.013}$	$0.068^{+0.041}_{-0.014}$	$0.127^{+0.029}_{-0.012}$	$0.079^{+0.050}_{-0.009}$	$0.086^{+0.019}_{-0.032}$	$0.051^{+0.032}_{-0.012}$	$0.088^{+0.016}_{-0.014}$
RELXILLCP	Norm (10^{-3})	1.23 ± 0.06	$2.31^{+0.10}_{-0.11}$	$5.30^{+0.25}_{-0.50}$	$6.54^{+0.20}_{-0.25}$	0.88 ± 0.05	5.0 ± 0.3	$5.27^{+0.17}_{-0.07}$
XILLVERCP	Norm (10^{-4})	$0.9^{+0.5}_{-0.6}$	$1.4^{+1.0}_{-0.9}$	6.9 ± 0.8	$7.5^{+1.0}_{-1.1}$	<0.5	$6.0^{+1.7}_{-2.9}$	2.9 ± 0.7
GAUSSIAN	σ (keV)	>0.054	>0.076	>0.088	...	>0.065	...	$0.059^{+0.019}_{-0.017}$
GAUSSIAN	Norm (10^{-4})	0.4 ± 0.3	1.1 ± 0.6	3.5 ± 0.9	...	$0.7^{+0.4}_{-0.5}$...	$3.2^{+0.6}_{-0.5}$
edge ₁	τ_{max}	$-0.030^{+0.020}_{-0.021}$	$-0.024^{+0.019}_{-0.018}$	-0.018 ± 0.009	...	$-0.053^{+0.029}_{-0.026}$...	$-0.026^{+0.006}_{-0.007}$
edge ₂	τ_{max}	$0.23^{+0.12}_{-0.06}$	$0.46^{+0.11}_{-0.14}$	$0.41^{+0.05}_{-0.06}$...	$0.12^{+0.09}_{-0.08}$...	0.40 ± 0.04
CRABCORR	$\Delta \Gamma_{\text{NICER}}$	0 (f)	0 (f)	0 (f)	...	0 (f)	...	0 (f)
CRABCORR	N_{NICER}	1 (f)	1 (f)	1 (f)	...	1 (f)	...	1 (f)
CRABCORR	$\Delta \Gamma_{\text{FPMA}}$	$0.097^{+0.020}_{-0.015}$...	$-0.013^{+0.010}_{-0.008}$	0 (f)	$0.022^{+0.021}_{-0.019}$	0 (f)	...
CRABCORR	N_{FPMA}	0.93 ± 0.03	...	$1.196^{+0.020}_{-0.019}$	1 (f)	1.36 ± 0.04	1 (f)	...
CRABCORR	$\Delta \Gamma_{\text{FPMB}}$	$0.102^{+0.020}_{-0.015}$...	$-0.039^{+0.011}_{-0.008}$	$-0.001^{+0.005}_{-0.006}$	0.017 ± 0.019	-0.012 ± 0.016	...
CRABCORR	N_{FPMB}	0.96 ± 0.03	...	$1.160^{+0.022}_{-0.026}$	1.021 ± 0.014	1.40 ± 0.04	$1.01^{+0.03}_{-0.04}$...
	L/L_{Edd}	0.3%	0.6%	1.8%	2.1%	0.3%	1.4%	1.6%
	PG-stat/dof				$6420.5/5789 = 1.11$			

Note. Errors are at the 90% confidence level and statistical only. The flux of the disk component is calculated using `cflux` in XSPEC. For the silicon line modeled by `gaussian`, the width is set to have an upper limit of 0.1 keV, and it is pegged at that upper limit in all epochs except for Epoch 7.

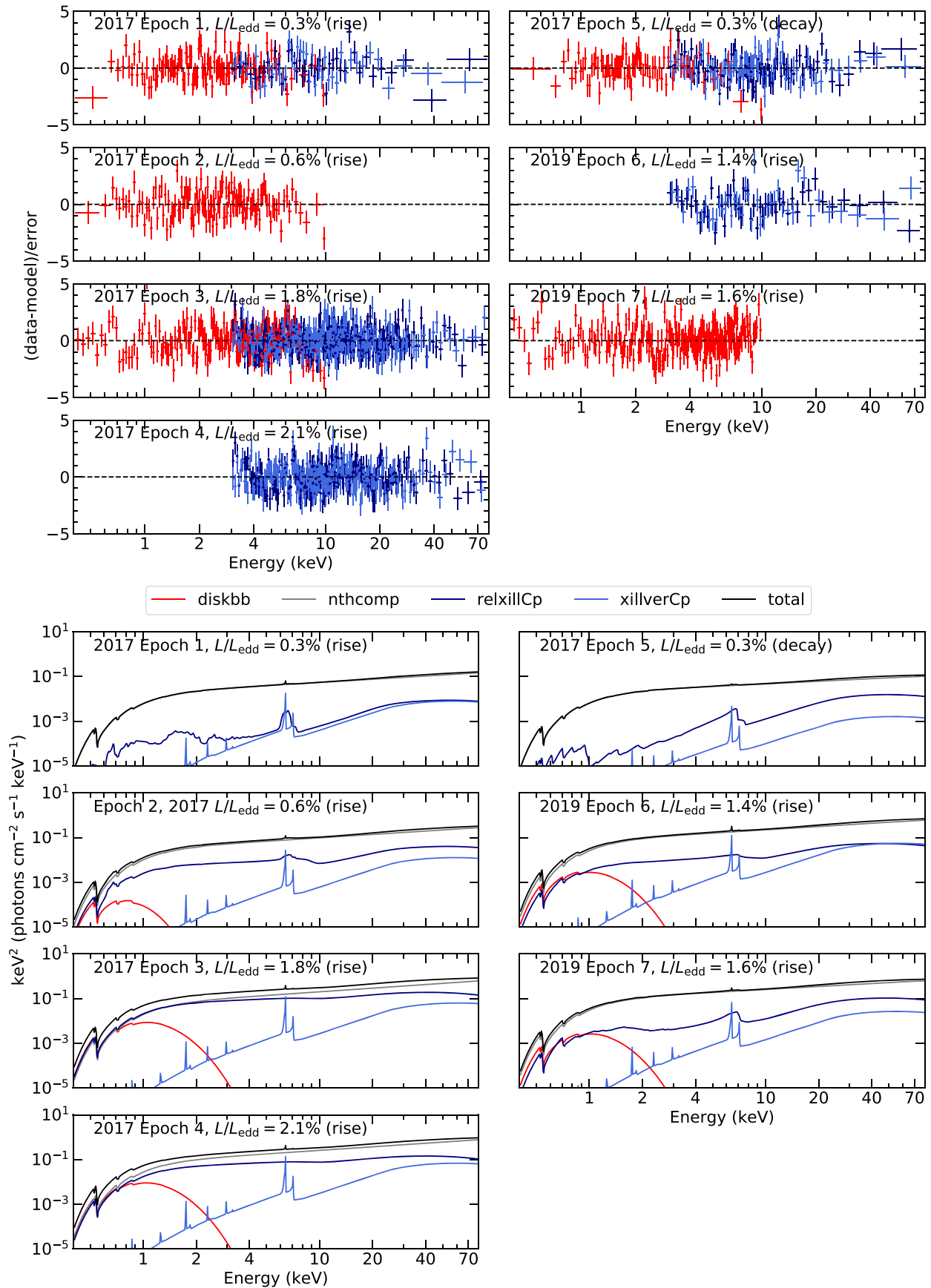


Figure 4. (Data-model)/error (upper) and model components (lower) for the simultaneous fit with the final complete model ($T_{\text{habs}} * \text{crabcorr} * (\text{diskbb} + \text{relxillCp} + \text{xillverCp} + \text{Gaussian}) * \text{edge} * \text{edge}$). In the ratio plot, red: NICER; navy: NuSTAR/FPMA; blue: NuSTAR/FPMB. Notice that the continuum component via nthcomp that is included in the relxillCp model is plotted separately from the reflection component. Also, the gaussian component that accounts for the calibration uncertainty is not shown, and all information about the calibration model is present in Table 2.

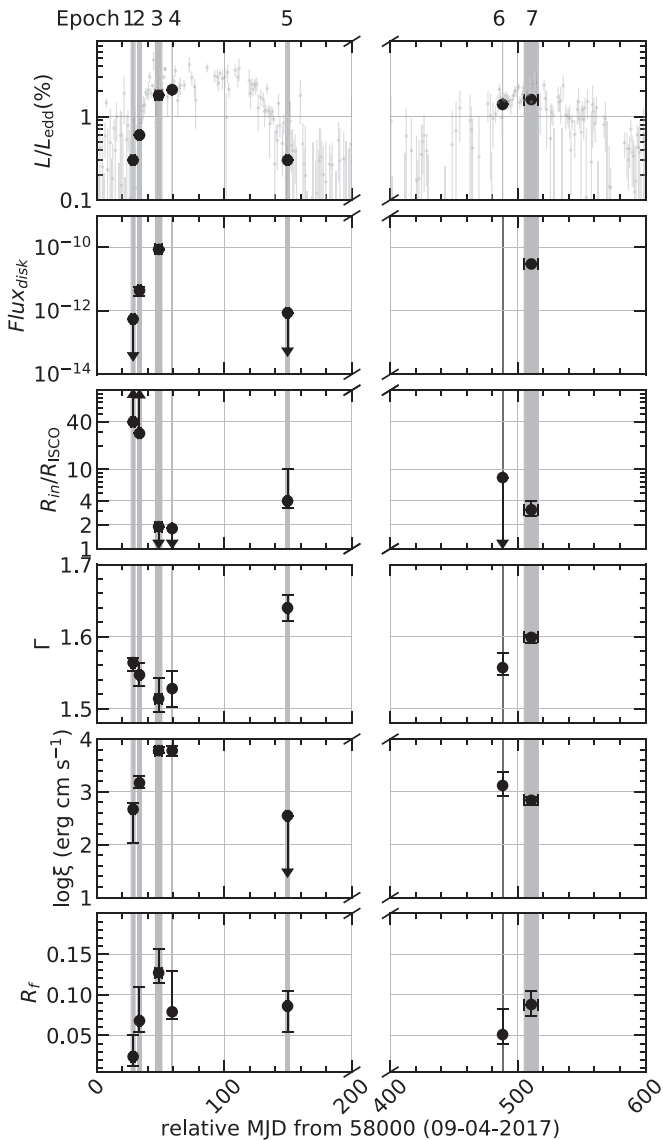


Figure 5. Best-fit evolution of disk properties during the 2017 and 2019 outburst cycles. Each epoch is shown with vertical shaded regions. In the top panel, the Swift/BAT light curve is overplotted to suggest the outbursts. The exact parameter values can be found in Table 2.

from a significant reduction of residuals at high energies seen by NuSTAR. A fixed solar iron abundance ($A_{\text{Fe}} = 1$) would increase PG-stat by 276. We note that the supersolar iron abundance problem could be potentially solved by adopting the high-density reflection model, as explored in Tomsick et al. (2018) and Jiang et al. (2019). Especially, Jiang et al. (2019) analyzed the same data set as in Wang-Ji et al. (2018) and obtained a close-to-solar iron abundance of $1.50_{-0.04}^{+0.12} A_{\text{Fe},\odot}$ and a high density in the disk surface of $\log(n_e/\text{cm}^{-3}) = 18.93_{-0.16}^{+0.12}$, while the density is fixed at $\log(n_e/\text{cm}^{-3}) = 15$ in the reflection model adopted in this work. We tested the high-density reflection model for Epoch 3 but found increased A_{Fe} . More details can be found in the Appendix.

3.3. Evolution of Physical Properties

In addition to these values of global parameters, we see clear evolution in the properties of the disk (see Figure 5). First, we

examine its evolution during the rise in 2017 (Epoch 1–4), when the luminosity increases from 0.3% to 2.1% L_{Edd} .

1. The inner radius of the disk only has a lower limit in Epochs 1 (>40 innermost stable circular orbit radius, hereafter R_{ISCO}) and 2 ($>28R_{\text{ISCO}}$), suggesting a large truncation radius of the disk, while in Epochs 3 and 4, with luminosities $\geq 1.8\% L_{\text{Edd}}$, $R_{\text{in}} < 2R_{\text{ISCO}}$. This trend is in line with the commonly agreed picture that the inner disk moves inward as the luminosity increases (Esin et al. 1997; Meyer-Hofmeister et al. 2005; Kylafis & Belloni 2015; Marcel et al. 2019).
2. The unabsorbed and unscattered flux from the disk component calculated using the model `cflux` in XSPEC increases, from $<5.5 \times 10^{-13}$ to $\sim 8.7 \times 10^{-11}$ $\text{erg cm}^{-2} \text{s}^{-1}$, by more than 2 orders of magnitude. In the meantime, the disk temperature is fixed at 50 eV in Epoch 1 and becomes ~ 100 and ~ 200 eV in Epochs 2 and 3, respectively.
3. The ionization parameter increases from $\log \xi$ (erg cm s^{-1}) = 2.7 to 3.8.
4. The reflection fraction R_f , which describes the fraction of reflected photons to those reaching the observer directly (Dauser et al. 2016), also increases from Epoch 1 (0.02) to 3 (0.13). This could be explained by a decreasing inner radius of the disk. In Epoch 4, the R_f is $0.079_{-0.009}^{+0.050}$, while the best-fit value is not as large as in Epoch 3, its 90% confidence upper limit is 0.13, consistent with R_f in Epoch 3.

Because of a larger effective area and longer exposure times, the NICER spectra have much better signal-to-noise ratios than Swift (which were used in Wang-Ji et al. 2018 and where disk evolution was difficult to determine), and we are now able to obtain reasonable and self-consistent evolution, which is predicted as the accretion disk’s inner radius moves inward between 0.3% and 2.1% L_{Edd} . One exception is the photon index Γ , which remains quite constant, and we will discuss this in Section 5.1.

Moreover, it is also worthwhile to compare results at the beginning and end of the 2017 outburst (Epochs 1 and 5), since, as mentioned earlier, the determined luminosities are similar, and both epochs have NICER and NuSTAR data for a broader energy coverage, taken during the rise and decay in the 2017 hard-only outburst. With the disk temperature fixed at 50 eV, the flux from the disk component during each epoch has a similar putative limit. The ionization has only an upper limit, $\log \xi$ (erg cm s^{-1}) < 2.55 . Also, the spectrum is slightly softer in the decay, with $\Gamma \sim 1.64$ compared to ~ 1.56 . This could be attributed to a difference in the optical depth in the corona. The most interesting difference is that during the decay, $R_{\text{in}} = 4.0_{-0.7}^{+6.1} R_{\text{ISCO}}$, while during the rise, the disk is largely truncated ($R_{\text{in}} > 40R_{\text{ISCO}}$). This difference naturally accounts for a reflection fraction \sim four times larger in Epoch 5 than in Epoch 1. The different level of disk truncation suggests a hysteresis effect during the rise and decay. It is worth noticing that if the inner radii in Epochs 1 and 5 are tied together, the PG-stat increases by 8, and $R_{\text{in}} > 36R_{\text{ISCO}}$. The confidence contours of $R_{\text{in},1}$ and $R_{\text{in},5}$ in the simultaneous fit suggest that they differ at the 2σ level. While alone, this is not statistically significant, we are encouraged by the simultaneous change in ionization and reflection fraction, all consistent with the hysteresis picture. If the hysteresis effect is real, then the lack

of a strong thermal component in Epoch 5 when the disk is only slightly truncated could be due to a low mass accretion rate.

In the 2019 hard-only outburst (Epochs 6 and 7, covered by NuSTAR and NICER, respectively), GX 339–4 has reached a lower peak luminosity (1.6% compared to 2.1% L_{Edd}). The inner disk radius is $\sim 3R_{\text{ISCO}}$, larger than in 2017. Meanwhile, the disk temperature (~ 180 eV) and unscattered flux from the disk component ($\sim 3 \times 10^{-11}$ cm $^{-2}$) are both slightly lower; the disk is less ionized, and the reflection fraction is also lower. Otherwise, we observe no significant differences between the 2017 and 2019 hard-only outbursts, considering the peak luminosity difference.

3.4. Other Emissivity Profiles

For the spectral fitting, we also tried emissivity profiles other than the canonical one that describes the intensity from the disk with $\propto r^{-3}$, including free emissivity indices and lamppost geometry. With emissivity indices free to vary, the PG-stat decreases by 34 with seven fewer dof, which is not a significant improvement. We can only constrain q to have upper or lower limits, except for Epoch 7, where $q = 4.1^{+1.2}_{-0.8}$; the iron abundance becomes even larger, $A_{\text{Fe}} = 6.3 \pm 0.7$, and the inclination is $42.6^{+1.2}_{-1.7}$. The most notable change is that the ionization parameter is less well constrained. The inner radius is unconstrained in Epoch 1 and slightly larger in Epochs 3 and 4 ($\sim 3R_{\text{ISCO}}$ compared to $\leq 2R_{\text{ISCO}}$), decreases to $< 1.6R_{\text{ISCO}}$ in Epoch 6 ($< 7.9R_{\text{ISCO}}$ in the $q = 3$ fit), and matches the $q = 3$ fit in the other three epochs.

With a lamppost geometry modeled by `relxilllpCp`, PG-stat is larger than the $q = 3$ fit by 76 with the same number of dof. The iron abundance drops slightly from ~ 4 to ~ 3 , as does the inclination ($\sim 38^\circ$ to $\sim 32^\circ$). We confirm the same trend in evolution with luminosity to the disk component and ionization. The predicted reflection fraction under the lamppost geometry also evolves with luminosity and is shifted to larger values (e.g., ~ 1.2 compared to ~ 0.13 in Epoch 3), which could help relax the requirement for the high coronal luminosity. Contour plots suggest that the lamppost height h is highly degenerate with the inner radius of the disk, so we are not able to determine these parameters independently from our data.

4. Time Lag Analysis with NICER Data

As introduced in Section 1, NICER is also a great instrument to conduct timing analysis, so we also explore the NICER data from a timing perspective. The epoch indexing is the same as in the spectral analysis, but here we only consider epochs with NICER coverage, namely, Epochs 1, 2, 3, 5, and 7.

In the 0.3–10 keV Poisson noise-subtracted power-density spectra, no quasi-periodic oscillations (QPOs) are detected. This is as expected, because a systematic QPO search (Motta et al. 2011) for GX 339–4 found no QPOs in the low-luminosity hard state. We notice that for Epochs 1 and 5, where the luminosity is lowest, Poisson noise becomes dominant above ~ 0.5 Hz, meaning that the signal-to-noise ratio is too low to extract any convincing results. In Epochs 2, 3, and 7, on the other hand, Poisson noise can be safely ignored at frequencies below 10, 30, and 20 Hz, respectively.

Following standard Fourier timing techniques (Uttley et al. 2014), we then calculate the cross-spectrum in each epoch, between the 0.5–1 and 1–10 keV energy bands, to obtain the

hard-to-soft lag spectra as a function of frequency. Using a standard logarithmic frequency rebinning with a factor of 0.4, the lag-frequency spectra in Epochs 2, 3, and 7 are shown in Figure 6, where we use the convention that a positive lag indicates a hard lag, meaning that the hard photons lag behind the soft photons. In all three epochs where Poisson noise can be safely ignored at frequencies below 10 Hz, a low-frequency hard lag is present, with its amplitude decreasing with frequency. This low-frequency hard lag can be fitted with a phenomenological power-law model (Nowak et al. 1999), and the indices are, in order of increasing luminosity, $-0.6^{+0.3}_{-0.2}$ (Epoch 2), $-1.5^{+0.1}_{-0.2}$ (Epoch 3), and -0.9 ± 0.1 (Epoch 7), suggesting that the low-frequency hard lag decreases with frequency faster when the luminosity is higher. The same trend was also found in previous time lag analysis work on GX 339–4 using XMM-Newton data (De Marco et al. 2015). At high frequencies in Epochs 3 (2–7 Hz) and 7 (4–8 Hz), we observe hints of soft lags that could be due to reverberation with millisecond amplitudes.

The energy-resolved lag spectra are obtained by calculating the cross-spectrum between each energy bin and a reference band (chosen to be 0.5–10 keV), following standard techniques in Uttley et al. (2014). From the low-frequency (0.1–0.5 Hz) lag-energy spectra in the three epochs where hard lags are confidently found, we see lags with large uncertainties in Epoch 2 limited by the low signal-to-noise ratio, whereas in Epochs 3 and 7, we find a log-linear dependence of lag on energy, but no clear difference between the epochs can be determined, considering the statistical errors.

At high frequencies, where we see the potential soft lags, we can use the lag-energy spectra to explore the reverberation picture. Figure 7 (lower) shows the high-frequency lag-energy spectra in Epochs 3 (2–7 Hz) and 7 (4–8 Hz). In Epoch 3, we see tentative hints of a thermal reverberation lag below 1 keV.

Since the uncertainties are quite large, it remains necessary to test the significance of the reverberation lag. If we fit the lag-energy spectrum with a power-law model with $\Gamma = 0$ (fixed), assuming that the hard lag due to propagating fluctuations can be safely ignored at these high frequencies, then the excess at 6.4 keV can be interpreted as an iron K lag. However, considering the large amplitude and uncertainty of the lag, we take the conservative approach and use a power-law model with a free Γ as the null hypothesis ($\Gamma = 1.0 \pm 0.4$ and $\chi^2/\text{dof} = 19.6/18 = 1.1$). Under this null hypothesis, the iron K lag is no longer significant ($< 1\sigma$ using an F-test), i.e., a nondetection.

For the thermal reverberation lag, it could be modeled with a `diskbb`, if it results from rethermalizing of the disk, and/or a `laor` model, if from a smeared iron L line. With our data, we cannot distinguish these two cases, but in either case, the significance of the thermal reverberation lag is above 2.5σ using an F-test. For consistency with the previous time lag analysis for the 2015 outburst with XMM-Newton data (De Marco et al. 2017), we estimate the thermal reverberation lag amplitude to be the maximum intensity of residuals above the extrapolation of the power-law model. The thermal reverberation lag found in this way is 9 ± 3 ms, which is consistent with the result therein. For instance, their highest luminosity is slightly lower than that in Epoch 3 (1.6% compared to 1.8% in Eddington units), and the thermal reverberation lag is 8 ± 3 ms in that observation.

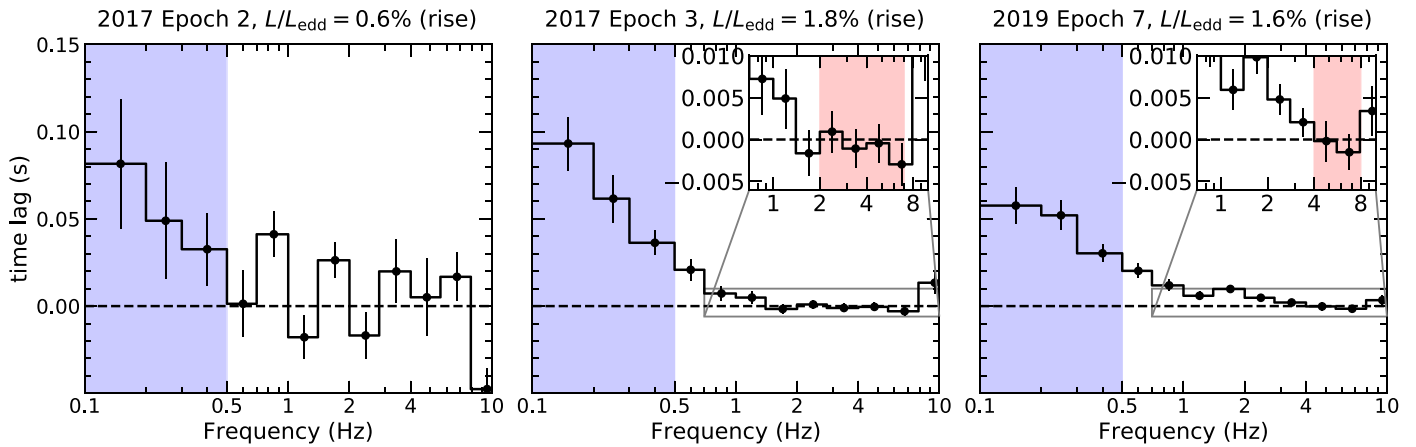


Figure 6. Lag-frequency spectra in the three epochs with NICER data. Poisson noise dominates above 10 Hz. The frequency range shaded in blue (0.1–0.5 Hz) is used to generate the low-frequency lag-energy spectra, resulting in a log-linear dependence of lag on energy in Epochs 3 and 7. The frequency ranges in the inserted zoomed-in lag-frequency spectra shaded in red are where potential candidates of a soft lag from reverberation are present. Those frequency ranges are used to generate the high-frequency lag-energy spectra in Figure 7.

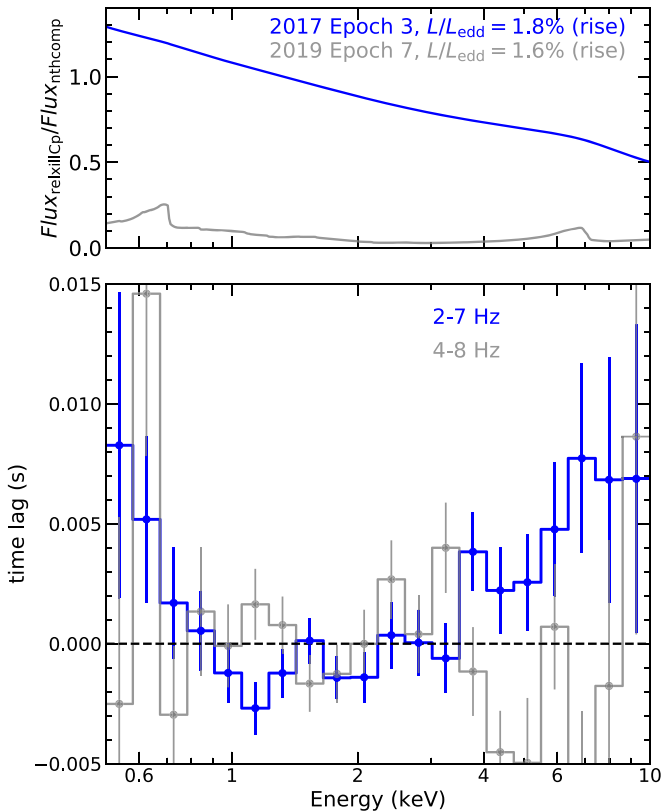


Figure 7. (Upper) Energy-resolved reflection fraction (reflection/continuum) illustrating the possibility that the reverberation lag is undetectable in Epoch 7 (gray) because the ratio of flux from the reflection component to the continuum is so much smaller than in Epoch 3 (blue), so that the dilution effect becomes larger. (Lower) High-frequency lag-energy spectra in the frequency range of 2–7 Hz in Epoch 3 and 4–8 Hz in Epoch 7. Tentative thermal and iron K-reverberation lags are seen in Epoch 3. See Section 4 for more details.

Epoch 7 reaches a luminosity slightly lower than Epoch 3 (1.6% versus 1.8% L_{Edd}), with a count rate lower by a factor of ~ 1.3 , but its effective exposure used in timing with a segment length of 10 s is larger by a factor of ~ 2.3 . For BHBs in the reverberation frequency region, the signal-to-noise ratio of the lag measurements scales with the count rate and the square root of the effective exposure (Uttley et al. 2014), resulting in a

signal-to-noise ratio of lag ~ 1.2 times larger in Epoch 7. In other words, we might statistically expect a soft X-ray lag in this epoch as well. However, as shown in the lag-energy spectrum of Epoch 7 (Figure 7, lower panel), there is no reverberation signature. This may be a consequence of the fact that the reflected photons represent a much smaller fraction of the X-ray emission in Epoch 7 than in Epoch 3 (see upper panel of Figure 7, where the flux ratio of the reflection and continuum components are shown). They are different by a factor of $\gtrsim 4$ both below 1 keV, where thermal reverberation could be seen, and at around 6.4 keV, where iron K reverberation could be present. A small fraction of reflected photons would lead to a larger dilution of reverberation lag, making it more difficult to observe. Also note that the ratio of flux from the reflection component to the continuum is related to but distinct from the reflection fraction R_f in Table 2 and Figure 5, which is defined as the ratio of coronal intensity that illuminates the disk and reaches the observer at infinity (see Dauser et al. 2016).

5. Discussion

5.1. Evolution of Inner Disk Radius and Possible Hysteresis Effects

We found that over the luminosity range of 0.3%–2.1% L_{Edd} , the inner disk radius moves inward, and the trends of disk component flux, ionization, and reflection fraction are consistent with what is expected. This coincides with an accretion flow increasing its radiative efficiency above $\sim 1\%$ L_{Edd} , which is both theoretically anticipated (e.g., see Yuan & Narayan 2014, Section 2.5) and supported by the change of slope in the radio/X-ray correlation (Coriat et al. 2011; Koljonen & Russell 2019). However, there are a few surprises from the spectral analysis.

From Figure 5, the photon index Γ does not show a clear correlation with the inner edge of the disk R_{in} , as would be expected if considering only the amount of cooling the corona gets from thermal disk photons. However, Γ is governed not only by the coronal temperature but also the coronal optical depth (Lightman & Zdziarski 1987). As mentioned in Section 3.1, our final fit assumes a fixed coronal temperature at 400 keV because previous endeavors found a pegged coronal temperature at that maximal value. This assumption

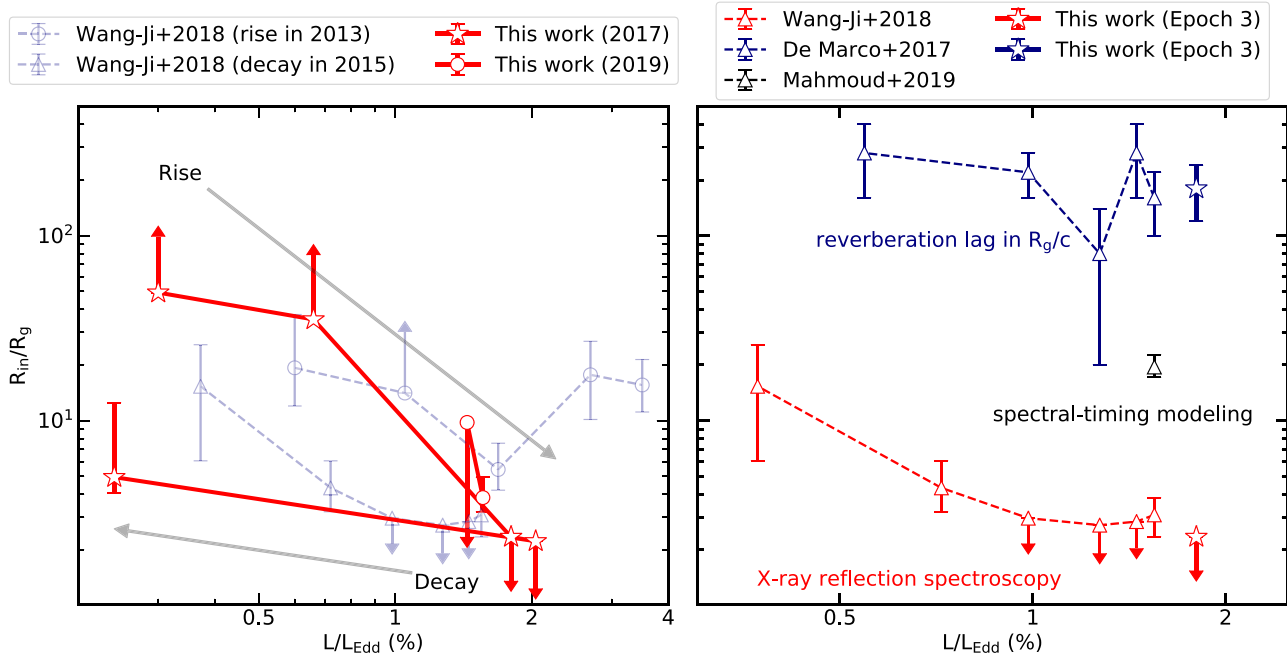


Figure 8. (Left) Comparison of the inner disk radius vs. Eddington-scaled luminosity for GX 339–4. Our best-fit values from reflection spectroscopy are shown in contrast with Wang-Ji et al. (2018). Notice that the R_{in} values in Table 2 are in units of R_{ISCO} , so a factor of 1.23 ($a_* = 0.998$) is corrected to be in R_g units. Two arrows show the evolution trend in the rise and decay phases, suggesting a hysteresis effect. (Right) Comparison of R_{in} obtained from reflection spectroscopy and the thermal reverberation lag amplitude in R_g/c units, from the analysis of the 2015 outburst data (De Marco et al. 2017; Wang-Ji et al. 2018) and this work. The Eddington ratio here assumes the unabsorbed flux in 1–100 keV, $d = 8$ kpc, and $M_{BH} = 10M_{\odot}$; i.e., the values in other works have been converted accordingly.

limits us from obtaining estimates of the optical depth. In García et al. (2015), where the coronal temperature and optical depth are both constrained, Γ does not show a simple correlation with R_{in} . The situation becomes even more complicated considering the unknown heating mechanism of the corona, i.e., how the accretion power gets dissipated into heating the corona to such high temperatures. We regard this as an important point, and one that needs to be reconciled in most physical pictures for the evolution of the inner edge of the accretion disk in the hard outburst.

We also notice that the change of the normalization of $xillverCp$ (N_x) is faster than the change of the total X-ray flux. For example, when comparing Epochs 4 and 5, the X-ray luminosity decreases by a factor of 7, while N_x decreases by a factor larger than 15. This could be due to an intrinsic change of coronal geometry, including both its size and location, irradiating a different solid angle of the disk at large radii. By generating contours between N_x and R_{in} using the STEPPAR command in XSPEC, we confirm that those two parameters are not correlated, so our results are not affected.

With our new measurements of R_{in} , we can extend the reported results on the evolution of R_{in} with luminosity in the hard state (e.g., García et al. 2015; Wang-Ji et al. 2018; García et al. 2019). The new results derived from NuSTAR and NICER, both free from pileup, agree with the picture that the inner radius moves inward as the luminosity increases in the hard state; in our four epochs with $L > 1\% L_{Edd}$, $R_{in} \leq 10R_g$, indicating that any truncation from the ISCO must be quite minor. At lower luminosities, as we mentioned in Section 3.3, the disk appears closer during the decay in comparison to the rise, suggesting a hysteresis effect. This idea is also supported by Wang-Ji et al. (2018), where we found that R_{in} was smaller in 2015 (decay) than in 2013 (rise) in the shared luminosity range (see the left panel in Figure 8).

We stress that even though the reflection spectra, especially the iron line shapes, are notably different in Epochs 1 and 5 during the rise and decay (see Figure 2), hysteresis is only marginally significant ($\Delta PG\text{-stat} = 8$ for one extra dof). Also, in the fit under the lamppost geometry, no hysteresis effect could be seen, but the PG-stat is worse by 76 with the same number of dof. However, the simultaneous change in ionization and reflection fraction suggests a hysteresis picture. If the hysteresis effect is real, possible physical interpretations include (1) different accretion modes at different mass accretion rates affected by the amount of Compton cooling or heating on the accretion disk (Meyer-Hofmeister et al. 2005), (2) the interplay of magnetic fields and the accretion flow (Petrucci et al. 2008; Begelman & Armitage 2014; Cao 2016), and (3) thermal limit cycles (Latter & Papaloizou 2012). More spectral-timing analysis for data with similar luminosity during the rise and decay is needed to further explore the hysteresis effect.

The paradigm where there is only a small level of disk truncation above $\sim 1\% L_{Edd}$ is challenged by observational evidence from both the spectral and timing sides. From the spectral side, the focus has shifted from pileup effects to model dependence; different models for reflection and the underlying continuum can lead to different inferred levels of disk truncation (Dzieřak et al. 2019). Using a high-density reflection model on the same data set as in Wang-Ji et al. (2018), Jiang et al. (2019) found higher upper limits on R_{in} for several epochs, e.g., $R_{in} < 8R_{ISCO}$ rather than $R_{in} = 1.8^{+3.0}_{-0.6}R_{ISCO}$, in an epoch with $L = 1.4\% L_{Edd}$. Mahmoud et al. (2019) used a double Comptonization model to account for temperature gradients in the inner-hot-flow-like corona. We have tested both the high-density reflection model and the double Comptonization model for Epoch 3 and found that the fit

statistics were not as good as our final model. More details can be found in the [Appendix](#).

5.2. Understanding Time Lags and the Need for Spectral-timing Modeling

From the timing side, one aspect of debate comes from converting the reverberation lag amplitude to a light travel time delay, i.e., between the corona and the reflecting inner disk. We can use our constraints on the amplitudes of thermal reverberation lags as an example to illustrate this (see [Figure 8](#)). In the most naive picture, the lag corresponds to a distance of $d = \tau c / (1 + \cos[\theta - i])$, where τ is the measured lag, and θ is the angle defining the location of the corona relative to the reflector ($\theta = 0$ represents a corona in the lamppost geometry and $\theta = \pi/2$ represents a central corona in a truncated disk geometry). Assuming a black hole mass of $10 M_{\odot}$ and an inclination angle of 38° , as we found with spectral fitting, a reverberation lag amplitude of 1 ms corresponds to a light travel time of $\sim 12R_g/c$ regardless of the exact value of θ . Then, our average thermal reverberation lag, 9 ± 3 ms, would correspond to a corona-to-inner disk distance of $108 \pm 36 R_g/c$. If considering dilution effects, the intrinsic lag would even be larger. For the same epoch (Epoch 3), R_{in} determined from energy spectral fitting is $< 2.4R_g$, leading to a large discrepancy.

The very large inferred truncation radius from reverberation lag amplitude is extreme and suggests that a direct conversion from lag amplitude to light travel distance between the corona and inner disk is not prudent. The primary reason is that even though the response function peaks at the disk truncation radius, which should be the same as inferred from the spectral fitting, it has a wing toward longer lags (i.e., the other parts of the disk also contribute to the measured ‘‘average’’ lag). In addition, there are secondary caveats. As we discussed in [Section 4](#), we cannot tell if any energy dependence in the hard lag is still present in the ‘‘high’’-frequency range we adopt (2–7 Hz). It is therefore possible that, limited by the signal-to-noise ratio, we are not probing frequencies high enough that reverberation lag becomes dominant. It is also worthwhile to note that in the recent work with NICER data on a bright BHB, MAXI J1820+070 ([Kara et al. 2019](#)), the averaged observed iron K-reverberation lag is 0.47 ± 0.08 ms, which is 1 order of magnitude smaller than ours and corresponds to $14 \pm 3R_g/c$. This reverberation lag amplitude is also the smallest measured so far in any BHB. However, the count rate reached by that source is $\sim 20,000$ counts s^{-1} , more than 100 times larger than that by GX 339–4 in these faint outbursts.

One promising approach to settle the discrepancy is to conduct a self-consistent spectral-timing analysis taking into account a proper transfer function. We notice that the two available spectral-timing models use a different approach to deal with the hard lag whose nature we do not understand yet. PROPFLUC ([Mahmoud & Done 2018a, 2018b](#); [Mahmoud et al. 2019](#)) assumes that the inner disk evaporates into a geometrically thick and hot flow that is radially stratified into a two-temperature continuum. This is one specific geometry of the disk corona, which makes PROPFLUC a bottom-up approach. On the other hand, the phenomenological hard lag treatment with the pivoting power law in the newly public model *reltrans* ([Ingram et al. 2019](#); [Mastroserio et al. 2019](#)) is a top-down approach, using which different theoretical predictions could be tested.

With *reltrans*, we could jointly fit the time-averaged spectrum and the real and imaginary parts of the energy-dependent cross-spectrum for a range of Fourier frequencies. The first X-ray reverberation mass measurement of a stellar-mass black hole is obtained with *reltrans* for Cygnus X-1 ([Mastroserio et al. 2019](#)). The fitted disk truncation radius is $< 10R_g$ at $\sim 1.6\% L_{Edd}$.

With the PROPFLUC model, [Mahmoud et al. \(2019\)](#) found that a truncation of $\sim 20R_g$ could explain the lag-energy spectra in three frequency bands and the power spectral densities in three energy bands. The observation used is the highest-luminosity observation in the 2015 outburst ($1.6\% L_{Edd}$). The thermal reverberation lag amplitude is 8 ± 3 ms ($96 \pm 36 R_g/c$ in light travel time, assuming $M_{BH} = 10M_{\odot}$ and an inclination of 38°). For the same observation but using Swift instead of XMM-Newton for soft energy coverage, reflection spectral fitting yields $R_{in} < 4R_g$ with 90% confidence ([Wang-Ji et al. 2018](#)). Even though the result from spectral timing still gives a large truncation of $20R_g$, it is much smaller than the reverberation lag in R_g/c units. It is much closer to the results from reflection spectroscopy but still shows a discrepancy.

6. Summary

We have analyzed seven epochs of GX 339–4 in the hard state seen by NICER and NuSTAR, five taken in the 2017 outburst and the other two during the rise of the 2019 outburst, with both outbursts being hard-only. The data cover a luminosity range of $0.3\%–2.1\% L_{Edd}$. Our major findings are as follows.

1. During the rise in 2017, the inner disk moves toward the ISCO radius, from $> 49R_g$ to $< 2R_g$. Other physical quantities show an evolution consistent with the R_{in} evolution, including a larger unscattered flux contribution from the thermal disk component (along with a higher disk temperature up to ~ 200 eV), an increasing ionization parameter, and an increasing reflection fraction (see [Figure 5](#)).
2. Epoch 5 has a similar luminosity as Epoch 1 but occurs during the decay; this observation shows a mild truncation at $\sim 5R_g$, while the reflection fraction is \sim four times larger, indicating a hysteresis effect during the rise and decay (see [Figure 8](#), left). The hysteresis effect has several physical interpretations and is potentially important for us to understand the accretion process and the mechanisms governing state transitions.
3. In our four epochs with $L > 1\% L_{Edd}$, we find that the disk is at most slightly truncated ($R_{in} \leq 10R_g$).
4. We observe a tentative thermal reverberation lag with an amplitude of 9 ± 3 ms, consistent with previous findings using XMM-Newton data. We also discussed possible reasons for the large discrepancy between the disk truncation level determined from spectral modeling and the large reverberation lag amplitude, assuming it comes from a light travel time delay between the corona and the inner disk. Possible reasons include contributions from reverberation from outer parts of the disk, the hard lags, and the soft-excess interpretation. Future spectral-timing modeling is needed to settle the discrepancy.

J.W., E.K., and J.A.G. acknowledges support from NASA grant 80NSSC17K0515 and thank the International Space Science Institute (ISSI) and participants of the ISSI Workshop

“Sombreros and Lampposts: The Geometry of Accretion onto Black Holes” for fruitful discussions. J.A.G. is thankful for support from the Alexander von Humboldt Foundation. E.M.C. gratefully acknowledges support from the National Science Foundation, CAREER award No. AST-1351222. R.M.L. acknowledges the support of NASA through Hubble Fellowship Program grant HST-HF2-51440.001.

Appendix

As discussed in Section 5.1, the choices of reflection model and underlying continuum shape can possibly change the result of the disk truncation radius. Therefore, we tested the double Comptonization (Mahmoud et al. 2019) and the high-density reflection model (Jiang et al. 2019) for Epoch 3, which has the highest-quality spectra. Our best-fit model is M1, $T_{\text{babs}}*\text{crabcorr}*(\text{diskbb}+\text{relxillCp}+\text{xillverCp}+\text{Gaussian})*\text{edge}*\text{edge}$; the double Comptonization model is M2, $T_{\text{babs}}*\text{crabcorr}*(\text{diskbb}+\text{relxillCp}+\text{relxillCp}+\text{Gaussian})*\text{edge}*\text{edge}$; and the high-density reflection model is $T_{\text{babs}}*\text{crabcorr}*(\text{relxillD}+\text{xillverD}+\text{Gaussian})*\text{edge}*\text{edge}$.

The treatment in M1 is the same as in our manuscript. For M2, $kT_{\text{e,hard}} = 100$ keV and $kT_{\text{e,soft}} = 35$ keV, as assumed in Mahmoud et al. (2019); in the second “soft” reflection component, only the normalization, photon index, and reflection fraction are untied from the “hard” reflection component. For M3, the parameters in `xillverD` are tied to `relxillD`, except that ionization is assumed to be $\log\xi = 0$, and the normalization is free to vary.

The resulting PG-stat/dof is $1690.0/1556 = 1.08$ for M1, $1721.9/1554 = 1.11$ for M2, and $1759.2/1557 = 1.13$ for M3. We notice that with M0, $T_{\text{babs}}*\text{crabcorr}*(\text{diskbb}+\text{relxillCp}+\text{Gaussian})*\text{edge}*\text{edge}$; PG-stat/dof is $1777.7/1557 = 1.12$, so M2 reduced PG-stat by 55.8 with three more dof, which is a great improvement but is still not as good as M1, which reduces PG-stat by 87.7 with only one more dof. We also check that if an extra distant reflection model component, `xillverCp`, is added to M2, the statistics is not improved; its normalization is $<3.4 \times 10^{-5}$, and it does not affect other parameters.

The best-fit parameters are shown in Table A1, and the model components and data-to-model ratios are in Figure A1. For M1, the individual fitting results are consistent with those shown in Table 2 for the simultaneous fitting in the manuscript,

Table A1
Best-fit Parameters for Our Best-fit Model M1, Double Comptonization Model M2, and High-density Reflection Model M3 in Epoch 3 (1.8% L_{Edd})

Model Component	Parameter	M1	M2	M3
RELXILLCP	a_*		0.988 (f)	
CRABCORR	$\Delta\Gamma_{\text{NICER}}$		0 (f)	
TBABS	N_{H} (10^{21} cm $^{-2}$)	6.32 ± 0.17	$6.72^{+0.08}_{-0.01}$	$5.55^{+0.08}_{-0.07}$
DISKBB	T_{in} (eV)	196^{+13}_{-10}	204^{+20}_{-10}	...
DISKBB	Norm (10^3)	$5.7^{+2.9}_{-2.1}$	$3.2^{+0.2}_{-0.7}$...
RELXILLCP/RELXILLD	q	>4.9	$6.0^{+0.9}_{-0.7}$	$8.0^{+1.5}_{-1.7}$
RELXILLCP/RELXILLD	i (deg)	$48.7^{+10.3}_{-7.7}$	$44.1^{+0.6}_{-0.7}$	$69.7^{+3.3}_{-6.0}$
RELXILLCP/RELXILLD	R_{in} (R_{ISCO})	$2.0^{+0.8}_{-0.5}$	$2.95^{+0.10}_{-0.09}$	<1.01
RELXILLCP/RELXILLD	Γ	$1.51^{+0.02}_{-0.07}$	$1.5710^{+0.0004}_{-0.0126}$	$1.364^{+0.024}_{-0.011}$
RELXILLCP/RELXILLD	$\log\xi$ (erg cm s $^{-1}$)	$3.80^{+0.10}_{-0.37}$	<2.01	3.49 ± 0.02
RELXILLCP/RELXILLD	A_{Fe}	$4.5^{+2.0}_{-0.50}$	8.8 ± 0.5	>9.5
RELXILLCP/RELXILLD	$\log N$ (cm $^{-3}$)	15 (f)	15 (f)	>18.7
RELXILLCP/RELXILLD	R_{f}	$0.12^{+0.08}_{-0.05}$	0.127 ± 0.003	$0.085^{+0.006}_{-0.002}$
RELXILLCP/RELXILLD	kT_{e} (keV)	400 (f)	100 (f)	...
RELXILLCP/RELXILLD	Norm (10^{-3})	5.4 ± 0.6	$5.491^{+0.008}_{-0.038}$	6.2 ± 0.3
XILLVERCP/XILLVERD	Norm (10^{-4})	$6.9^{+2.6}_{-2.3}$...	$5.5^{+0.9}_{-1.0}$
RELXILLCP _{soft}	Γ_{soft}	...	$3.20^{+0.04}_{-0.01}$...
RELXILLCP _{soft}	$R_{\text{f,soft}}$...	(u)	...
RELXILLCP _{soft}	$kT_{\text{e,soft}}$ (keV)	...	35 (f)	...
GAUSSIAN	E (keV)	1.85 ± 0.04	1.88 ± 0.04	1.91 ± 0.04
GAUSSIAN	σ (keV)	>0.089	$0.19^{+0.03}_{-0.02}$	>0.096
GAUSSIAN	Norm (10^{-4})	3.6 ± 1.0	$7.8^{+1.0}_{-0.9}$	4.7 ± 0.9
edge ₁	E (keV)	$2.29^{+0.05}_{-0.06}$	2.3 ± 0.03	$2.28^{+0.03}_{-0.04}$
edge ₁	τ_{max}	-0.023 ± 0.011	-0.050 ± 0.006	-0.062 ± 0.010
EDGE ₂	E (keV)	$0.532^{+0.007}_{-0.008}$	$0.534^{+0.003}_{-0.004}$	0.533 ± 0.008
EDGE ₂	τ_{max}	$0.42^{+0.07}_{-0.06}$	$0.415^{+0.046}_{-0.013}$	$0.36^{+0.07}_{-0.06}$
CRABCORR	$\Delta\Gamma_{\text{FPMA}}$	-0.018 ± 0.015	0.022 ± 0.012	$0.0186^{+0.014}_{-0.017}$
CRABCORR	N_{FPMA}	$1.189^{+0.016}_{-0.028}$	$1.271^{+0.022}_{-0.003}$	1.26 ± 0.03
CRABCORR	$\Delta\Gamma_{\text{FPMB}}$	-0.044 ± 0.015	-0.0043 ± 0.0012	$-0.008^{+0.012}_{-0.017}$
CRABCORR	N_{FPMB}	1.15 ± 0.03	1.233 ± 0.003	1.225 ± 0.003
	PG-stat/dof	$1690.0/1556 = 1.08$	$1721.9/1554 = 1.11$	$1759.2/1557 = 1.13$

Note. Errors are at the 90% confidence level and statistical only.

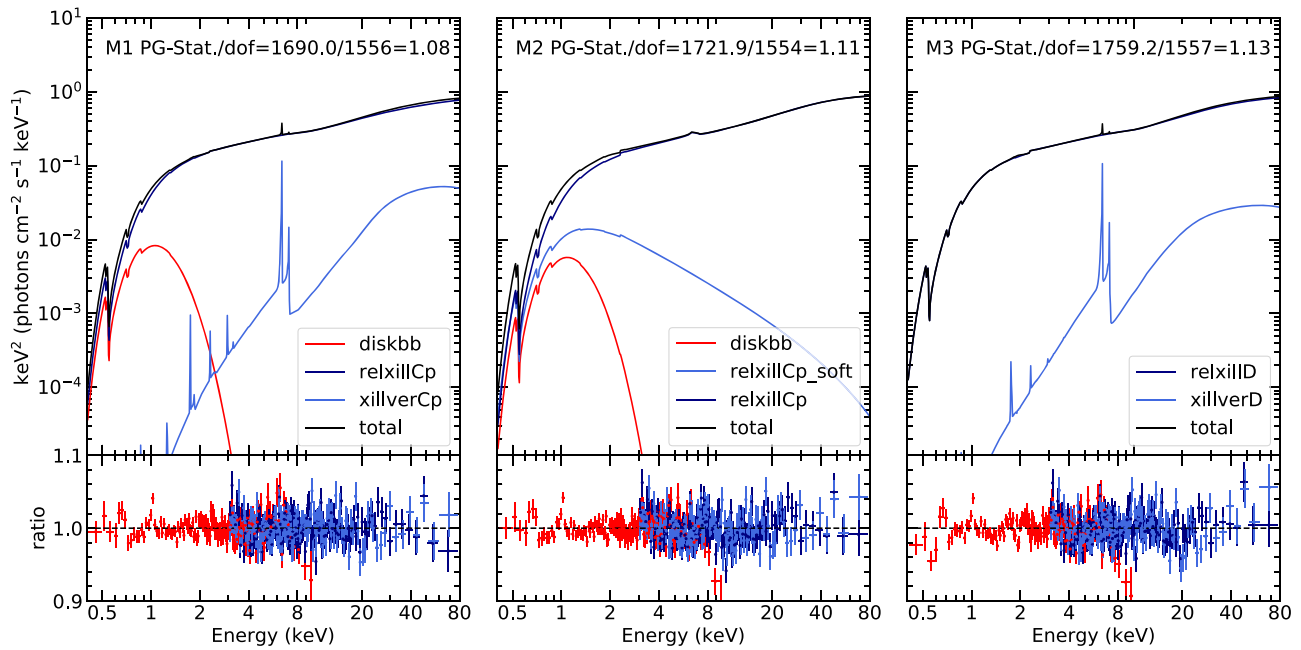


Figure A1. Model components (upper) and data-to-model ratio (lower) for the fit with the final model M1, the double Comptonization model M2, and the high-density model M3. In the plot, red: NICER; navy: NuSTAR/FPMA; and blue: NuSTAR/FPMB.

except that the emissivity index $q > 4.9$ here, while we fix it at 3 in the manuscript. However, fixing q at 3 here would only increase the PG-stat by 3.3, which means the spectrum is insensitive to properly constrain q , and the value of q would not affect the fit. As for M2, the disk truncation level ($R_{\text{in}} = 2.95^{+0.10}_{-0.09} R_{\text{ISCO}}$) is similar to M1, instead of being more largely truncated, as suggested in Mahmoud et al. (2019). Also, the double Comptonization model does not return a closer-to-solar iron abundance. In fact, the iron abundance is increased in M2 (~ 8.8) compared to M1 (~ 4.5).

Regarding M3, the disk component is no longer required because high-density reflection could add a quasi-blackbody emission in the soft band below 2 keV, as suggested in Jiang et al. (2019). The inclination is $\sim 70^\circ$, which is much higher than in M1 and M2, and the spectrum is much harder, with $\Gamma \sim 1.36$. The iron abundance is pegged at a maximal value of 10, and $R_{\text{in}} < 1.01 R_{\text{ISCO}}$; both trends are inconsistent with Jiang et al. (2019). However, we notice that in M3 here, we use the high-density reflection model `relxillD`, which means that we are limited by the higher limit of density of $\log(N/\text{cm}^{-3}) = 19$, and the fitted density is pegged at this higher limit ($\log(N/\text{cm}^{-3}) > 18.7$), while Jiang et al. (2019) found $\log(N/\text{cm}^{-3}) = 20.6$ with the reflection model `reflionx`. Therefore, the changes of iron abundance and disk inner radius when a high density is considered still need investigation with more atomic data with high electron densities.

ORCID iDs

Jingyi Wang <https://orcid.org/0000-0002-1742-2125>
 Erin Kara <https://orcid.org/0000-0003-0172-0854>
 James F. Steiner <https://orcid.org/0000-0002-5872-6061>
 Javier A. García <https://orcid.org/0000-0003-3828-2448>
 Jeroen Homan <https://orcid.org/0000-0001-8371-2713>
 Joseph Neilsen <https://orcid.org/0000-0002-8247-786X>
 Grégoire Marcel <https://orcid.org/0000-0003-1780-5641>
 Renee M. Ludlam <https://orcid.org/0000-0002-8961-939X>

Francesco Tombesi <https://orcid.org/0000-0002-6562-8654>
 Edward M. Cackett <https://orcid.org/0000-0002-8294-9281>
 Ron A. Remillard <https://orcid.org/0000-0003-4815-0481>

References

- Arévalo, P., & Uttley, P. 2006, *MNRAS*, 367, 801
 Arnaud, K. A. 1996, in ASP Conf. Ser. 101, *Astronomical Data Analysis Software and Systems V*, ed. G. H. Jacoby & J. Barnes (San Francisco, CA: ASP), 17
 Bambi, C. 2017, *Black Holes: A Laboratory for Testing Strong Gravity* (Berlin: Springer)
 Basak, R., & Zdziarski, A. A. 2016, *MNRAS*, 458, 2199
 Begelman, M. C., & Armitage, P. J. 2014, *ApJ*, 782, L18
 Bogdanov, S. 2019, AAS Meeting, 233, 426.02
 Cao, X. 2016, *ApJ*, 817, 71
 Cassatella, P., Uttley, P., Wilms, J., & Poutanen, J. 2012, *MNRAS*, 422, 2407
 Coriat, M., Corbel, S., Prat, L., et al. 2011, *MNRAS*, 414, 677
 Dauser, T., García, J., Walton, D., et al. 2016, *A&A*, 590, A76
 De Marco, B., & Ponti, G. 2016, *ApJ*, 826, 70
 De Marco, B., Ponti, G., Muñoz-Darias, T., & Nandra, K. 2015, *ApJ*, 814, 50
 De Marco, B., Ponti, G., Petrucci, P., et al. 2017, *MNRAS*, 471, 1475
 Done, C., & Diaz Trigo, M. 2010, *MNRAS*, 407, 2287
 Done, C., Gierliński, M., & Kubota, A. 2007, *A&ARv*, 15, 1
 Dzielak, M. A., Zdziarski, A. A., Szanecki, M., et al. 2019, *MNRAS*, 485, 3845
 Esin, A. A., McClintock, J. E., & Narayan, R. 1997, *ApJ*, 489, 865
 Fabian, A., Rees, M., Stella, L., & White, N. E. 1989, *MNRAS*, 238, 729
 Fabian, A., Zoghbi, A., Ross, R., et al. 2009, *Natur*, 459, 540
 Fender, R. P., Belloni, T. M., & Gallo, E. 2004, *MNRAS*, 355, 1105
 Gandhi, P., Altamirano, D., Russell, D., et al. 2017, *ATel*, 10798, 1
 García, J., Dauser, T., Lohfink, A., et al. 2014, *ApJ*, 782, 76
 García, J. A., Steiner, J. F., McClintock, J. E., et al. 2015, *ApJ*, 813, 84
 García, J. A., Tomsick, J. A., Sridhar, N., et al. 2019, *ApJ*, 885, 48
 Gendreau, K. C., Arzoumanian, Z., Adkins, P. W., et al. 2016, *Proc. SPIE*, 9905, 99051H
 Harrison, F. A., Craig, W. W., Christensen, F. E., et al. 2013, *ApJ*, 770, 103
 Heida, M., Jonker, P., Torres, M., & Chianassa, A. 2017, *ApJ*, 846, 132
 Ingram, A., Mastroserio, G., Dauser, T., et al. 2019, *MNRAS*, 488, 324
 Jiang, J., Fabian, A. C., Wang, J., et al. 2019, *MNRAS*, 484, 1972
 Kara, E., Alston, W. N., Fabian, A. C., et al. 2016, *MNRAS*, 462, 511
 Kara, E., Steiner, J., Fabian, A., et al. 2019, *Natur*, 565, 198
 Koljonen, K. I., & Russell, D. M. 2019, *ApJ*, 871, 26

- Krimm, H. A., Holland, S. T., Corbet, R. H., et al. 2013, *ApJS*, 209, 14
- Kylafis, N., & Belloni, T. 2015, *A&A*, 574, A133
- Latter, H. N., & Papaloizou, J. C. 2012, *MNRAS*, 426, 1107
- Lightman, A. P., & Zdziarski, A. A. 1987, *ApJ*, 319, 643
- Ludlam, R., Miller, J., Arzoumanian, Z., et al. 2018, *ApJL*, 858, L5
- Ludlam, R., Miller, J., & Cackett, E. 2015, *ApJ*, 806, 262
- Lyubarskii, Y. E. 1997, *MNRAS*, 292, 679
- Mahmoud, R. D., & Done, C. 2018a, *MNRAS*, 473, 2084
- Mahmoud, R. D., & Done, C. 2018b, *MNRAS*, 480, 4040
- Mahmoud, R. D., Done, C., & De Marco, B. 2019, *MNRAS*, 486, 2137
- Marcel, G., Ferreira, J., Clavel, M., et al. 2019, *A&A*, 626, A115
- Mastroserio, G., Ingram, A., & van der Klis, M. 2019, *MNRAS*, 488, 348
- McHardy, I., Arévalo, P., Uttley, P., et al. 2007, *MNRAS*, 382, 985
- McHardy, I. M., Papadakis, I., Uttley, P., Page, M., & Mason, K. 2004, *MNRAS*, 348, 783
- Meyer-Hofmeister, E., Liu, B., & Meyer, F. 2005, *A&A*, 432, 181
- Miller, J., Homan, J., Steeghs, D., et al. 2006, *ApJ*, 653, 525
- Miyamoto, S., & Kitamoto, S. 1989, *Natur*, 342, 773
- Motta, S., Muñoz-Darias, T., Casella, P., Belloni, T., & Homan, J. 2011, *MNRAS*, 418, 2292
- Nowak, M. A., Vaughan, B. A., Wilms, J., Dove, J. B., & Begelman, M. C. 1999, *ApJ*, 510, 874
- Papadakis, I., Nandra, K., & Kazanas, D. 2001, *ApJL*, 554, L133
- Parker, M., Tomsick, J., Kennea, J. A., et al. 2016, *ApJL*, 821, L6
- Petrucci, P.-O., Cabanac, C., Corbel, S., Koerding, E., & Fender, R. 2014, *A&A*, 564, A37
- Petrucci, P.-O., Ferreira, J., Henri, G., & Pelletier, G. 2008, *MNRAS: Letters*, 385, L88
- Plant, D., Fender, R., Ponti, G., Muñoz-Darias, T., & Coriat, M. 2015, *A&A*, 573, A120
- Reis, R., Fabian, A., Ross, R., et al. 2008, *MNRAS*, 387, 1489
- Remillard, R. A., & McClintock, J. E. 2006, *ARA&A*, 44, 49
- Reynolds, C. S. 2013, *CQGra*, 30, 244004
- Russell, D. M., Lewis, F., & Gandhi, P. 2017a, *ATel*, 10797, 1
- Russell, T., Tetarenko, A., Sivakoff, G., & Miller-Jones, J. 2017b, *ATel*, 10808, 1
- Steiner, J. F., García, J. A., Eikmann, W., et al. 2017, *ApJ*, 836, 119
- Steiner, J. F., McClintock, J. E., Remillard, R. A., et al. 2010, *ApJL*, 718, L117
- Tetarenko, B., Sivakoff, G., Heinke, C., & Gladstone, J. 2016, *ApJS*, 222, 15
- Tomsick, J. A., Kalemci, E., Kaaret, P., et al. 2008, *ApJ*, 680, 593
- Tomsick, J. A., Parker, M. L., García, J. A., et al. 2018, *ApJ*, 855, 3
- Tomsick, J. A., Yamaoka, K., Corbel, S., et al. 2009, *ApJL*, 707, L87
- Uttley, P., Cackett, E., Fabian, A., Kara, E., & Wilkins, D. 2014, *A&ARv*, 22, 72
- Uttley, P., Wilkinson, T., Cassatella, P., et al. 2011, *MNRAS: Letters*, 414, L60
- Van der Klis, M., Hasinger, G., Stella, L., et al. 1987, *ApJ*, 319, L13
- Vaughan, B., Van der Klis, M., Lewin, W., et al. 1994, *ApJ*, 421, 738
- Verner, D., Ferland, G., Korista, K., & Yakovlev, D. 1996, *ApJ*, 465, 487
- Wang-Ji, J., García, J. A., Steiner, J. F., et al. 2018, *ApJ*, 855, 61
- Wilms, J., Allen, A., & McCray, R. 2000, *ApJ*, 542, 914
- Yuan, F., & Narayan, R. 2014, *ARA&A*, 52, 529
- Zdziarski, A. A., Johnson, W. N., & Magdziarz, P. 1996, *MNRAS*, 283, 193
- Zdziarski, A. A., Poutanen, J., Mikolajewska, J., et al. 1998, *MNRAS*, 301, 435
- Zoghbi, A., Fabian, A., Reynolds, C., & Cackett, E. 2012, *MNRAS*, 422, 129
- Życki, P. T., Done, C., & Smith, D. A. 1999, *MNRAS*, 309, 561